Structure−Property Relationships of Pt−Sn Nanoparticles Supported on Al_2O_3 for the Dehydrogenation of Methylcyclohexane

Kazumasa Murata [†], *Natsuki Kurimoto* [†], *Yuta Yamamoto*[‡], *Akira Oda* [†,‖], *Junya Ohyama*[§,‖], *Atsushi Satsuma** [†,‖]

† Graduate School of Engineering, Nagoya University, Nagoya 464-8603, Japan

‡ Institute of Materials and Systems for Sustainability, Nagoya University, Nagoya, Japan

§ Faculty of Advanced Science and Technology, Kumamoto University, Kumamoto 860-8555, Japan

‖Elements Strategy Initiative for Catalysts and Batteries (ESICB), Kyoto University, Katsura, Kyoto 615-8520, Japan

KEYWORDS

Pt−Sn catalyst, dehydrogenation, methylcyclohexane, nanoparticle, alloy, local structure

ABSTRACT

The structure−catalytic property relationships of Al_2O_3 supported Pt−Sn nanoparticles (Pt−Sn/Al_2O_3) in the dehydrogenation of methylcyclohexane (MCH) were investigated by varying the Sn/Pt ratios of the catalysts. The initial activity and the deactivation rate of the Pt−Sn/Al_2O_3 catalysts in the MCH dehydrogenation decreased in line with an increase in the Sn/Pt ratio from 0 to 3. The Pt−Sn/Al_2O_3 catalyst with a Sn/Pt ratio of 2 showed good activity, durability, and toluene selectivity in the MCH dehydrogenation among the catalysts. The dispersion of Pt in the Pt−Sn/Al_2O_3 catalysts was observed to decrease with an increase in the Sn/Pt ratio. Structural changes in the catalysts from Pt−Sn clusters to intermetallic Pt_3Sn and PtSn nanoparticles were also observed using scanning transmission electron microscopy (STEM) and X-ray diffraction (XRD). According to structural analysis using X-ray absorption fine structure (XAFS) spectroscopy and infrared (IR) spectroscopy using carbon monoxide as a probe, the electron density of Pt increased and the fraction of Pt−Pt adjacent sites decreased with an increase in the Sn/Pt ratio. Comparing the catalytic properties and the structures of the Pt−Sn/Al_2O_3 catalysts, their initial activities were correlated with the dispersion of Pt. In addition, the durability and selectivity of the catalysts were enhanced due to an increase in the electron density of Pt and a decrease in the number of Pt−Pt adjacent sites. Overall, the properties of the catalysts in the MCH dehydrogenation are determined by the local structure of Pt atoms rather than the crystal structure of the Pt−Sn alloy nanoparticles on Al_2O_3.

1. INTRODUCTION

Supported Pt nanoparticles have been widely used in the dehydrogenation of alkanes to preferentially activate C−H bonds rather than C−C bonds. However, supported Pt catalysts are rapidly deactivated by coke which is formed as a byproduct of dehydrogenation reaction. Therefore, secondary metals such as Sn and Ga are often added to the Pt catalysts to improve their activity, selectivity, and durability. In terms of supported Pt−Sn catalysts, their active phase depends on the preparation conditions[5–8] and support materials.[9–14] The Sn/Pt ratio also plays an important role in controlling the structure of Pt−Sn nanoparticles and the interaction between Pt and Sn. Optimizing the Sn/Pt ratio leads to an improvement in the performance of the catalyst in the dehydrogenation of alkanes. Although a wide range of Sn/Pt ratios of Pt−Sn/Al_2O_3 catalysts, from 1/4 to 5, has been selected for the dehydrogenation of alkanes, the optimal Sn/Pt ratio remains controversial.[9,10,15–24] This is due to the Sn species being not only involved in the formation of an alloy with Pt, but also being dispersed on the metal oxide support. In terms of the supported Pt−Sn catalysts for the dehydrogenation of alkanes that have so far been reported, Lee et al. reported that the dehydrogenation activity of Pt−Sn/Al_2O_3 with an Sn/Pt ratio of 5/2 was the highest due to the formation of a PtSn alloy.[16] However, Ding et al. found that Pt−Sn/SiO_2 with an Sn/Pt ratio of 1 showed the highest activity in the dehydrogenation of propane, and that a Pt_3Sn alloy was more active than its PtSn counterpart.[6,25] Furukawa et al. reported that 9 nm Pt_3Sn particles supported on SiO_2 were highly active in the dehydrogenation of cyclohexane and n-butane compared to catalysts featuring Pt and PtSn particles of the same size.[26] Wu et al. found that the turnover frequency (TOF) and ethylene selectivity of Pt−Sn particles for the dehydrogenation of ethane increased with increasing the Sn/Pt ratio of the catalyst from 0 to 1/3.[27] However, previous reports have also shown that dispersed Pt−Sn clusters are highly active species in the dehydrogenation of alkanes.[9,11,22] These reports suggest that the catalytic properties of the Pt−Sn catalysts toward the

dehydrogenation of alkanes are partially dependent on their crystal structures, but not directly connected to them.

To elucidate the factors that control the dehydrogenation properties of supported Pt−Sn particle catalysts, it is necessary to investigate the local structure of the Pt atoms, which is modified by the Sn. It is well known that adding Sn to supported Pt catalysts to modify their electronic and geometric structures has a positive effect on the properties of the catalysts toward the dehydrogenation of alkanes.[7,9,14,28] The enhancements of activity, selectivity, and durability of Pt−Sn catalysts are the result of the strong electronic interaction that occurs between Sn and Pt.[9,14] In addition, the geometric arrangements of atoms, such as in isolated Pt sites, Pt_3 hollow sites, and Pt_4 ensemble sites of Pt alloy nanoparticles also affect the selectivity and durability of the catalyst in the dehydrogenation of alkanes.[28,29] However, the relationship between the particle size, crystal, electronic, and geometric structure of supported Pt−Sn catalysts and their activity, selectivity, and durability has not been fully discussed in the literature. An understanding of these relationships would provide fundamental insights into supported Pt−Sn alloy catalysts for use in the dehydrogenation of alkanes and enable more rational design of catalysts.

As an important chemical reaction in the petrochemistry and polymer synthesis, the dehydrogenation of alkanes to alkenes has been studied in great detail over a long period of time.[1,2] Recently, methylcyclohexane (MCH), commonly referred to as an organic hydride, has received much attention as a hydrogen carrier,[3] as it has the desirable properties of a relatively high boiling point (101 °C) and low melting point (−126 °C), which allow it to be stably transported and stored as a liquid.[4] In addition to this, the relatively high H_2 storage capacity, low toxicity, and reusability of MCH make it a very versatile compound. The MCH dehydrogenation is typically achieved

under ambient pressure, at a temperature in the range of 300–400 °C, to produce toluene (TOL) and three equivalents of hydrogen, according to the reaction (MCH → TOL + $3H_2$).

Herein, the structure and catalytic properties of Pt−Sn/Al_2O_3 catalysts were systematically investigated for the dehydrogenation of MCH by changing the Sn/Pt ratios within the range of 0–3. The sizes, crystal structures, and chemical compositions of Pt−Sn alloy particles on Al_2O_3 supports were found to be dependent on the Sn/Pt ratio. The geometric and electronic structures of Pt−Sn/Al_2O_3 were characterized using X-ray absorption fine structure (XAFS) and Fourier-transform infrared (FT-IR) spectroscopies. A comparison of the structures and catalytic properties revealed that the local structures of the Pt−Sn/Al_2O_3 catalysts control the MCH dehydrogenation.

2. EXPERIMENTAL

2.1. Catalyst preparation

Scheme S1 shows schematic representation of preparation method of the Pt−Sn/Al_2O_3 catalysts. The Al_2O_3 support was obtained via the thermal decomposition of boehmite (Sasol, PURAL alumina) at 600 °C for 1 h. Pt (Pt loading: 2 wt%) and Sn (Sn loading: 0.24–3.7 wt%) were deposited onto the prepared Al_2O_3 support via a co-impregnation method using $H_2PtCl_6 \cdot 6H_2O$ and $SnCl_2 \cdot 2H_2O$ precursors (Kishida Chemical Co., Ltd.). Al_2O_3 supports were simultaneously impregnated with aqueous solutions of $H_2PtCl_6 \cdot 6H_2O$ and $SnCl_2 \cdot 2H_2O$, and then the suspensions were stirred for 1 h. As soon as their aqueous solutions were mixed, the suspensions changed from yellow to yellowish-brown. This color maybe derived from a $[PtCl_2(SnCl_3)_2]^{2-}$ complex.[30,31] Excess water from the suspensions was removed using a rotary evaporator at 60 °C, and then the

catalysts were dried at 80 °C for 8 h and calcined at 500 °C for 3 h. Prior to the characterization and the catalytic testing, the catalysts were reduced under a flowing of H_2 at 600 °C for 30 min. Different Sn/Pt ratios were used to obtain various Pt−Sn(x/y)/Al_2O_3 catalysts, where x/y is the molar ratio of Sn to Pt, where the Pt and Sn loading and Sn/Pt ratio values for each catalyst can be found to be listed in Table 1. Pt/Al_2O_3 (Pt loading: 2 wt%) and Sn/Al_2O_3 (Sn loading: 1.2 wt%) was prepared using the same impregnation method as a control catalyst.

2.2. CO pulse chemisorption

Carbon monoxide (CO) pulse chemisorption measurements were performed using a BEL-CAT-B instrument (MicrotracBEL). Approximately 50 mg of sample was placed in a sample tube and then pretreated under 100% H_2 at 600 °C for 30 min. After the sample was allowed to cool to 50 °C under a He atmosphere, CO pulse chemisorption measurements were carried out using a mixture of 5% CO/He while monitoring the effluent using a thermal conductivity detector. The dispersion of Pt was calculated based on the total volume of gases adsorbed, under the assumption that CO was adsorbed on the Pt surface in a 1:1 (Pt:CO) stoichiometry.

2.3. X-ray diffraction (XRD)

XRD measurements were carried out using a Rigaku ATX-G diffractometer equipped with a Cu Kα radiation source.

2.4. Scanning/transmission electron microscopy (S/TEM)

The catalysts were exposed to a 10% H_2/N_2 atmosphere at 600 °C for 30 min. Samples were prepared for TEM and STEM by spreading a drop of a methanol suspension of the pretreated catalysts. TEM, STEM, and energy-dispersive X-ray spectroscopy (EDS) were performed on a JEOL JEM-2100F field emission electron microscope operated at 200 kV. The catalyst structure was observed in detail by spherical aberration-corrected (Cs-)STEM and electron energy loss spectroscopy (EELS) using a JEOL JEM-ARM200F double aberration-corrected high-resolution scanning transmission electron microscope operated at 200 kV.

2.5. XAFS

Pt L_3- and Sn K-edge XAFS measurements were carried out at room temperature on the BL5B1 and BL11S2 beamlines of Aichi Synchrotron Radiation Center in Aichi, Japan, respectively. The samples were pretreated under an atmosphere of 10% H_2/N_2 for 30 min at 600 °C, after which they were sealed under N_2 at room temperature so that XAFS spectra could be recorded without any exposure of the samples to the air. Data analysis of the samples was performed using the Athena and Artemis software including in the Demeter package.

2.6. X-ray photo electron spectroscopy (XPS) measurement

The XPS measurement was conducted using an ESCALAB250 X-ray photoelectron spectrometer (Thermo Fisher Scientific). The catalysts were exposed to a 10% H_2/N_2 atmosphere at 600 °C for

30 min. The binding energy of the surface Sn species were modified by contaminated carbon as internal standard. The C 1s binding energy of carbon was defined to 284.8 eV.

2.7. Fourier-transform infrared (FT-IR) spectroscopy

FT-IR measurements were performed using a quartz *in situ* IR cell and a JASCO FT/IR-6100 spectrometer (JASCO Co.) equipped with a liquid nitrogen-cooled HgCdTe (MCT) detector. FT-IR spectra were obtained via the averaging of 128 scans (ca. 120 sec) at a resolution of 4 cm^{-1}. Approximately 50 mg of samples were formed into the self-supporting disk and then placed in an IR cell with a CaF_2 window. The samples were pretreated under a 10% H_2/Ar atmosphere at a rate of 100 mL min^{-1} at 600 °C for 30 min and were then cooled to 50 °C under Ar, and IR spectra were taken as a background. CO (0.4% CO/Ar at a rate of 100 mL min^{-1}) was then introduced into the quartz *in situ* IR cell for 10 min. The CO physisorbed on the samples was then removed under a flow of 100% Ar, and the IR spectra of the samples with adsorbed CO were obtained.

2.8. Catalytic testing of the MCH dehydrogenation

The dehydrogenation of MCH was carried out under atmospheric pressure in a conventional fixed-bed flow reactor. Catalyst samples were pressed into pellets, crushed, and sieved into 300–600 μm grains. The catalyst grains (10 mg) were placed inside a U-shaped quartz tube with an inside diameter of 4 mm; The height of the catalyst bed was about 3 mm. Prior to conducting the activity tests, the samples were exposed to a flowing mixture of 10% H_2/Ar for 30 min at 600 °C. The MCH dehydrogenation was then performed at 300 °C under a 1.6% MCH/Ar atmosphere at a total

flow rate of 100 mL min^{-1}, corresponding to a gas hourly space velocity (GHSV) of 600,000 mL g^{-1} h^{-1}. MCH was introduced into the tube under the bubbling of Ar gas through a saturator maintained at 0 °C. The reaction products were analyzed every 20 min by an online Shimazu Nexis GC-2030 gas chromatograph equipped with two dielectric-barrier discharge ionization detectors (BID), with one BID attached to an Rt-Msieve 5A capillary column (0.32 mm × 15 m) to detect H_2 and methane (CH_4) and the other BID attached to an Rt®-Q-BOND capillary column (0.32 mm × 30 m) to detect MCH and TOL. The MCH conversion, TOL selectivity, and initial TOF (at 5min) of the catalysts were calculated through the following equations (1)–(3).

$$\text{MCH conversion (\%)} = \frac{\text{TOL concentration (\%)}}{\text{MCH concentration (\%)} + \text{TOL concentration (\%)}} \times 100 \qquad (1)$$

$$\text{TOL selectivity (\%)} = \frac{\text{TOL concentration (\%)}}{\text{TOL concentration (\%)} + \text{CH}_4\text{ concentration (\%)}} \times 100 \qquad (2)$$

$$\text{Initial TOF } (s^{-1}) = \frac{\text{MCH flow rate (mol s}^{-1}) \times \text{Initial MCH conversion (at 5 min) (\%)}}{\text{Mole of Pd atoms in the catalyst (mol)} \times \text{Pd dispersion (\%)}} \qquad (3)$$

The deactivation rate of the catalysts was calculated via a pseudo-first-order approximation of the time course of the MCH conversion.

3. RESULTS and DISCUSSION

3.1. Dispersions of Pt and particle sizes

Table 1 shows the dispersions of Pt in the Pt/Al_2O_3 and $Pt–Sn/Al_2O_3$ catalysts estimated from the CO pulse chemisorption measurements. It can be seen that the dispersion of Pt in Pt/Al_2O_3 is

63.0% which is the highest among those of the Pt−Sn/Al_2O_3 samples. As the Sn/Pt ratio increased from 1/5 to 3, the dispersion of Pt in the Pt−Sn/Al_2O_3 catalysts decreased from 44.2% to 11.9%.

Table 1. Sn/Pt composition, dispersion of Pt, and particle size of each catalyst. The catalyst samples pretreated under a flow of H_2 at 600 °C for 30 min.

catalyst	Pt content (wt%)	Sn content (wt%)	Sn/Pt ratio	Pt dispersion[a] (%)	particle size[b] (nm)
Pt/Al_2O_3	2.0	−	0	63.0	1.0
Pt−Sn(1/5)/Al_2O_3	2.0	0.24	1/5	44.2	1.0
Pt−Sn(1/3)/Al_2O_3	2.0	0.41	1/3	41.3	2.2
Pt−Sn(1)/Al_2O_3	2.0	1.2	1	38.5	5.3
Pt−Sn(2)/Al_2O_3	2.0	2.4	2	22.3	4.7
Pt−Sn(3)/Al_2O_3	2.0	3.7	3	11.9	6.4

[a]Pt dispersion calculated from CO pulse chemisorption, [b]number-average particle size estimated from TEM images.[32]

Figure S1 shows the TEM images and particle size distributions for Pt/Al_2O_3 and the different Pt−Sn/Al_2O_3 samples. It can be seen that the Pt/Al_2O_3 catalyst features only Pt nanoparticles that are smaller than 2 nm in size (defined as clusters in this study) and has a monomodal size distribution with a maximum particle size of 1 nm. These results correspond to the high Pt dispersion (63.0%) of Pt/Al_2O_3. The size distribution of Pt−Sn(1/5)/Al_2O_3 is similar to that of Pt/Al_2O_3. The TEM image of Pt−Sn(1/3)/Al_2O_3 shows that the sample contains some

nanoparticles that are >5 nm in size. At an Sn/Pt ratio of 1 or more, numerous particles with >5 nm in size were observed on the Al_2O_3. The Pt−Sn/Al_2O_3 samples show a bimodal size distribution, with maxima at 1 and 8 nm. Thus, the decrease in the dispersion of Pt can be explained as being a result of the formation of larger particles upon an increase in the Sn/Pt ratio. Although small clusters of around 1 nm and particles with >5 nm in size are comparable in terms of the number of particles they contain, the number of atoms in the particles is actually more than a hundred times greater than that in the clusters. Thus, Pt−Sn/Al_2O_3 samples with an Sn/Pt ratio of ≥1 predominantly have larger particles of >5 nm in size. STEM−EDS mapping was then used to determine the locations of the Pt and Sn atoms on Al_2O_3 in the different samples (Figure S2). The EDS mapping of Pt/Al_2O_3 shows that it contains no Pt aggregates. However, in the case of the Pt−Sn/Al_2O_3 samples, the signals of Pt and Sn can be observed to be overlapped in the elemental mapping of the particles that are >5 nm in size showing that these nanoparticles formed upon the addition of Sn are alloy particles that contain both Pt and Sn atoms. From these results, larger Pt−Sn particles are probable to be formed when they interact more strongly with Sn species than the Al_2O_3 support in the catalyst preparation via the impregnation method. In addition, the data shows that some Pt and Sn atoms were highly dispersed on Al_2O_3, corresponding to the small clusters of <2 nm in size present in the Pt−Sn/Al_2O_3 samples.

3.2. Crystalline structure

XRD was used to identify the crystal structure of the nanoparticles in the Pt−Sn/Al_2O_3 samples. Figure 1 shows the XRD patterns of the Pt−Sn/Al_2O_3 samples compared with those of the Al_2O_3 support and Pt/Al_2O_3. The XRD pattern of Pt/Al_2O_3 was found to be very similar to that of Al_2O_3.

This was also the case for the Pt−Sn/Al_2O_3 samples with an Sn/Pt ratio of ≤1/3, with their patterns being very similar to that of Al_2O_3 indicating that Pt and Sn are highly dispersed on the Al_2O_3 support in these samples. These results indicated that Pt and Sn are highly dispersed on the Al_2O_3 support in these samples. For the Pt−Sn(1)/Al_2O_3, a shoulder can be observed on a peak in its XRD pattern at around 38.9°, which can be attributed to the formation of intermetallic Pt_3Sn alloy.[5–7,26,27] For the Pt−Sn(2)/Al_2O_3, there is an increase in the intensity of the peak related to intermetallic Pt_3Sn compared to that in the pattern of the Pt−Sn(1)/Al_2O_3. In addition, in the XRD pattern of the Pt−Sn(2)/Al_2O_3, there are several small peaks at 25.0, 30.0, 41.8, and 44.1° that can be attributed to the formation of intermetallic PtSn alloy.[5–7,26] Therefore, it was determined that Pt_3Sn alloy particles are mainly formed in the Pt−Sn(1)/Al_2O_3 and Pt−Sn(2)/Al_2O_3 samples. In the case of the Pt−Sn(3)/Al_2O_3 sample, the increase in the intensity of the peaks attributed to PtSn was observed in line with an increase in the Sn/Pt ratio. However, the intensity of the diffraction peaks of Pt_3Sn significantly decreased. In other words, in Pt−Sn(3)/Al_2O_3, PtSn alloy particles are preferentially formed over Pt_3Sn alloy particles. Moreover, the XRD patterns of Sn metal or Sn oxide were not detected in the patterns of any of the samples.

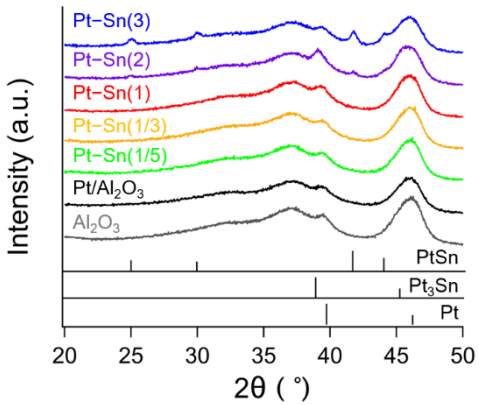

Figure 1. XRD patterns of the Pt/Al_2O_3 and $Pt–Sn/Al_2O_3$ catalysts with different Sn/Pt ratios, alongside reference Pt (space group $Fm\bar{3}m$), Pt_3Sn (space group $Pm\bar{3}m$), and PtSn (space group $P6_3/mmc$) peaks. The catalyst samples pretreated under a flow of H_2 at 600 °C for 30 min.

The structures of the $Pt–Sn/Al_2O_3$ catalysts were studied in detail using Cs-STEM–EELS mappings. Figure 2a shows a Cs-STEM image of a large nanoparticle of >5 nm in size in $Pt-Sn(1)/Al_2O_3$, which exhibits a lattice fringe that can be attributed to a (100) facet of intermetallic Pt_3Sn. In the EELS mapping and the line scanning profile of $Pt–Sn(1)/Al_2O_3$ shown in Figure 2b and c, the high fraction of Pt in the Pt_3Sn particle of the sample is reflected in the fact that the signal of the Sn $M_{4,5}$-edge is much weaker compared to that of the Pt $M_{4,5}$-edge. In contrast, lattice fringes attributed to (102) and (201) facets of intermetallic PtSn can be observed in the Cs-STEM image of the $Pt–Sn(3)/Al_2O_3$, as shown in Figure 2d. In the line scanning profile, the signal of the Sn $M_{4,5}$-edge is comparable to that of the Pt $M_{4,5}$-edge, supporting the presence of PtSn alloy particles rich in Sn in $Pt–Sn(3)/Al_2O_3$ rather than Pt_3Sn alloy particles, as shown in Figures 2e and f. Furthermore, Cs-STEM images of Pt/Al_2O_3 and $Pt–Sn(1/3)/Al_2O_3$ show small Pt or Pt–Sn clusters with irregular atomic arrangements (Figure S3).

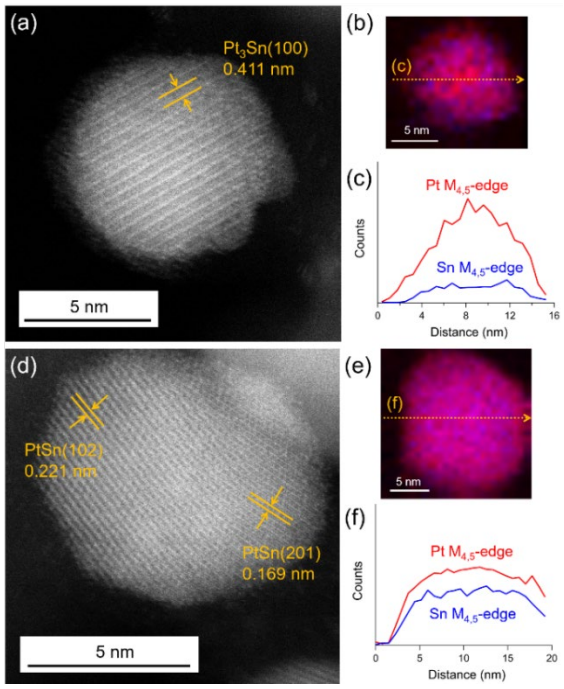

Figure 2. (a,d) Cs-STEM images, (b,e) EELS mappings, and (c,f) line scanning profiles of >5 nm in size nanoparticles of (a–c) Pt−Sn(1)/Al_2O_3 and (d–f) Pt−Sn(3)/Al_2O_3. The catalyst samples pretreated under a flow of H_2 at 600 °C for 30 min.

3.3. Electronic and geometric structures

The Pt L_3-edge X-ray absorption near edge structure (XANES) spectra of Pt/Al_2O_3 and Pt−Sn/Al_2O_3 is shown in Figure 3a. The XANES spectrum of Pt/Al_2O_3, which is similar to that of Pt foil, indicates that the Pt clusters present on Al_2O_3 are in the metallic state. In detail, the white line intensity of Pt/Al_2O_3 at 11567 eV is slightly higher than that of the Pt foil, reflecting that cationic Pt species resulting from the charge transfer from Pt to Al_2O_3 at their interface.[33,34] In the case of the Pt−Sn/Al_2O_3 catalysts, the white line intensity at around 11567 eV decreased with an increase in the Sn/Pt ratio. The relative electron density in the Pt 5d orbitals was evaluated

from the peak area of the white line in the XANES spectra (Figures 4 and S4),[35–37] where a decrease in the peak area indicates an increase in the electron density of the Pt 5d orbitals. Upon an increase in the Sn/Pt ratio of the Pt−Sn/Al_2O_3 catalysts, a decrease in the white line peak area was gradually observed. Thus, electron transfer from Sn to Pt was shown to occur upon the formation of Pt−Sn alloy particles.[7,9,38]

Figures 3b and c show the Pt L_3-edge EXAFS and Fourier transforms (FTs) of the EXAFS spectra, respectively. In the FT of the EXAFS spectrum of Pt/Al_2O_3, scattering peaks due to Pt−O and Pt−Pt can be observed at around 1.6 and 2.5 Å, respectively. The coordination numbers of Pt−O and Pt−Pt were estimated from the curve fitting of the EXAFS spectrum and are presented in Table S1. The coordination number of Pt−Pt of 5.7 is close to the previously reported value for Pt/Al_2O_3 containing Pt particles that are around 1 nm in size.[33,39–41] The EXAFS spectra of Pt−Sn(3)/Al_2O_3 could be well fitted by assuming that there are three scattering peaks attributed to Pt−O, Pt−Pt, and Pt−Sn that have coordination numbers of 0.7, 2.6, and 1.8, respectively (Table S1). However, for the Pt−Sn/Al_2O_3 catalysts with Sn/Pt ratios of ≤2, it was difficult to obtain good fitting results due to the suppression of the scattering peak at around 2.5 Å in their spectra, which can be attributed to the interference of the EXAFS oscillations of Pt−Pt and Pt−Sn.[18–20] Therefore, the formation of Pt−Sn alloys was also suggested to occur in the other Pt−Sn/Al_2O_3 catalysts.

Figure S5a shows the Sn K-edge XANES spectra, where it can be observed that the XANES spectra of the Pt−Sn/Al_2O_3 catalysts are similar to the XANES spectrum of SnO. From this data, the average oxidation number of Sn in the Pt−Sn/Al_2O_3 catalysts was inferred to be approximately +2.[7,9,13,14,18] To confirm the presence of Sn^0 in the intermetallic Pt−Sn alloys, the Sn 3d XPS measurements were conducted using Pt−Sn/Al_2O_3 (Figure S6). According to XPS measurements, the Sn species were the Sn^0 of ca. 30% and the Sn^{2+}/Sn^{4+} of ca. 70% in all the

Pt–Sn/Al_2O_3 catalysts. Figures S2b and c show the Sn K-edge EXAFS spectra and their corresponding FTs. The scattering peak of Sn–O at around 1.5 Å suggests the presence of highly dispersed SnO_x species on the Al_2O_3 support. In spite of the formation of Pt–Sn alloy particles, as indicated by the XRD and STEM results, no scattering peaks for Sn and Pt atoms adjacent to Sn atoms were observed at 2–3 Å, as a result of the interference of the scattered electrons by the Sn and Pt atoms adjacent to the Sn atoms.[18] Based on the XRD, STEM, and XAFS results, it was proposed that dispersed SnO_x (Sn^{2+}/Sn^{4+}) species and Pt–Sn alloy particles containing Sn^0 coexist on the Al_2O_3 support in the Pt–Sn/Al_2O_3 catalysts.[23]

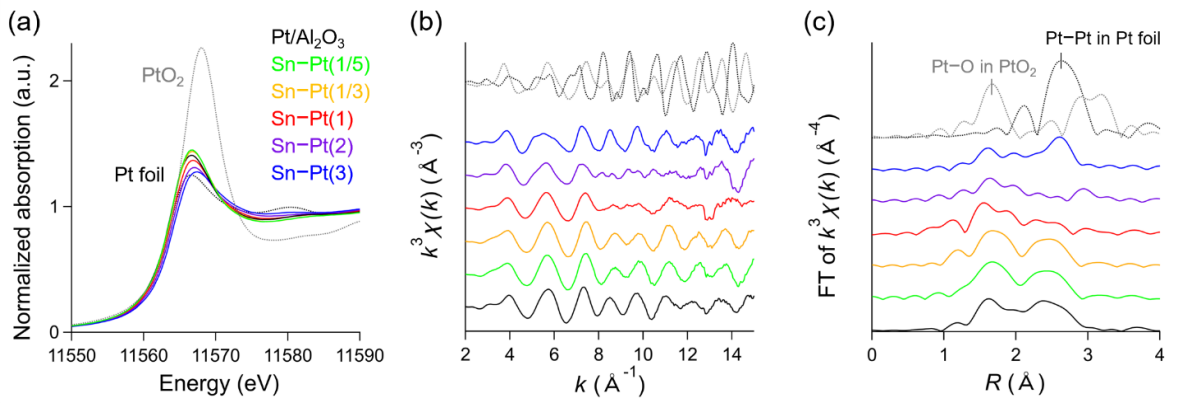

Figure 3. Pt L_3-edge (a) XANES, (b) EXAFS, and (c) FTs of the EXAFS spectra for the Pt/Al_2O_3 and Pt–Sn/Al_2O_3 catalysts. The black and gray dotted lines indicate the Pt foil and PtO_2 references, respectively. The catalyst samples pretreated under a flow of H_2 at 600 °C for 30 min.

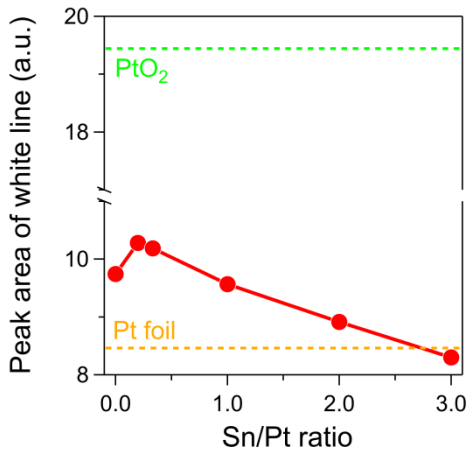

Figure 4. Peak area of the white line from the Pt L_3-edge XANES spectra of Pt−Sn/Al_2O_3 catalysts with different Sn/Pt ratios.

Figure 5 shows the FT-IR spectra of CO adsorbed on Pt/Al_2O_3 and the different Pt−Sn/Al_2O_3 catalysts. In the FT-IR spectrum of Pt/Al_2O_3, three CO stretching vibration bands can be observed at 2126, 2068, and 1844 cm^{-1}. The strongest band at 2068 cm^{-1} was assigned to the linear adsorbed CO on Pt^0,[17,21,24,33,39,42–48] and the weak bands at 2126 and 1844 cm^{-1} were attributed to the linear adsorbed CO on $Pt^{\delta+}$ [42–44] and bridge adsorbed CO on Pt^0 [17,33,39,44,46–48], respectively. In line with an increase in the Sn/Pt ratio of the Pt−Sn/Al_2O_3 catalysts, the decrease in the intensities of the bands at 2126 and 1844 cm^{-1} can be observed. The former implies a decrease in the number of highly dispersed Pt clusters that interact strongly with the Al_2O_3, whereas the latter indicates the disappearance of the ensembles of Pt−Pt atoms as a result of the generation of Pt−Sn alloy particles. In the FT-IR spectrum of Pt−Sn (3)/Al_2O_3, the band at 1844 cm^{-1} can barely be observed and that at around 2068 cm^{-1} is slightly shifted compared with the same bands in the spectra of the other catalysts in response to the change in the electronic state of

the surface Pt atoms. The red shifts in the IR band suggest that Pt becomes more electron-rich upon an increase in the Sn/Pt ratio of the Pt−Sn/Al_2O_3 catalysts (Figure S7), which is similar to the trend observed in the change in the Pt L_3-edge XANES spectra. To quantify the fraction of Pt surface sites, fitting of the FT-IR spectra was performed using a Gaussian function (Figure S8). Figure 6 shows the fraction of linear and bridge adsorbed CO on Pt^0 for the Pt−Sn/Al_2O_3 catalysts versus the Sn/Pt ratio. The fraction of the linear adsorbed CO increased from 0.88 to 0.97 with increasing the Sn/Pt ratio from 0 to 3, while that of the bridge adsorbed CO decreased monotonically from 0.12 to 0.03. Therefore, the addition of Sn atoms into the catalysts diluted the Pt nanoparticles, thus reducing the fraction of Pt−Pt adjacent sites.

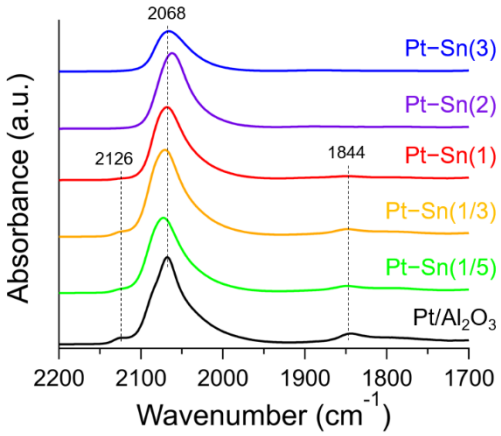

Figure 5. FT-IR spectra of CO adsorbed on Pt/Al_2O_3 and the different Pt−Sn/Al_2O_3 catalysts. The catalyst samples pretreated under a flow of H_2 at 600 °C for 30 min.

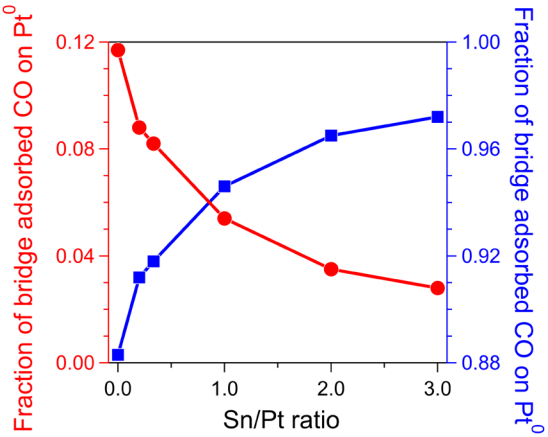

Figure 6. Plots of the fractions of bridge and linear adsorbed CO on Pt^0 in the Pt−Sn/Al_2O_3 catalysts versus the Sn/Pt ratio.

Scheme 1 shows a schematic diagram of the structures of the Pt−Sn nanoparticles in the Pt−Sn/Al_2O_3 catalysts according to the different Sn/Pt ratios based on the structural analysis. The macroscopic structures of the catalysts were determined by CO pulse chemisorption, XRD, and STEM. For the catalysts with Sn/Pt ratios of 1/5 and 1/3, Pt−Sn clusters of <2 nm in size are mainly present on the Al_2O_3, while Pt_3Sn particles are formed when the Sn/Pt ratio increases to 1 and 2. With a further increase in the Sn/Pt ratio to 3, the Pt_3Sn particles convert to PtSn particles. As the Sn/Pt ratio increases, the particle size in the Pt−Sn/Al_2O_3 catalysts increases and the dispersion of the Pt decreases from 63.0% to 11.9%. The addition of Sn to supported Pt catalysts modifies the local structure of the Pt atoms. The electronic and geometric structures of Pt−Sn/Al_2O_3 were characterized by using XAFS and FT-IR spectroscopy. It was found that the electron density of Pt in the Pt−Sn/Al_2O_3 catalysts increased due to the interaction between the Pt and Sn atoms, as shown in Figure 4. The number of Pt ensemble sites, corresponding to Pt−Pt adjacent sites for

bridge CO adsorption, on the Pt−Sn/Al_2O_3 decreases in line with an increase in the Sn/Pt ratio (Figure 8).

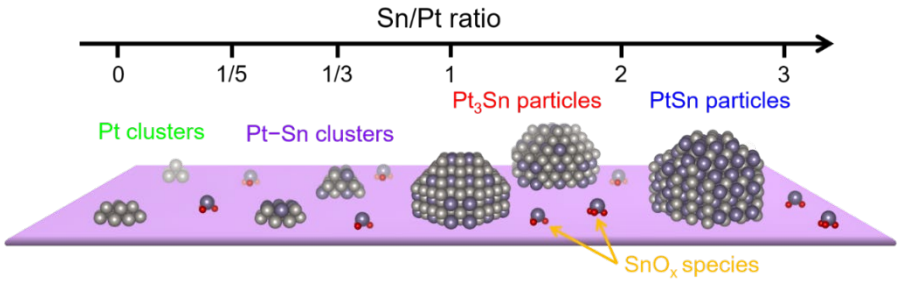

Scheme 1. Schematic diagram of the variation in the structures of Pt−Sn nanoparticles in the Pt−Sn/Al_2O_3 catalysts according to their different Sn/Pt ratios.

3.4. Catalytic performance of the MCH dehydrogenation

The MCH dehydrogenation was carried out under atmospheric pressure at 300 °C using the different Pt−Sn/Al_2O_3 catalysts. Figures 7a and b show the time courses of the MCH conversion and the TOL selectivity for Pt/Al_2O_3 and the different Pt−Sn/Al_2O_3 catalysts. The catalytic parameters were summarized in the Table S2. The gas and heat diffusions have little effect on the catalytic reaction due to relatively low MCH conversions (<50%). According to repeating activity tests, experimental error for MCH conversion was ca. 5% (Figure S9). Comparing the initial MCH conversions after 5 min for all of the catalysts, Pt/Al_2O_3 was found to show the highest MCH conversion of 44.0%. The initial MCH conversions of the Pt−Sn/Al_2O_3 catalysts decreased from 37.1% to 11.2% according to an increase in the Sn/Pt ratio (Figure S10a). H_2, CH_4, and TOL were

detected as products of the MCH dehydrogenation, where the H_2: TOL ratio was approximately 3:1. CH_4 is thought to be generated as a result of the demethylation of TOL, while no other gas-phase products were detected upon the dehydrogenation of MCH. To investigate the role of SnO_x in dehydrogenation of MCH, we tested the activity of Sn/Al_2O_3 catalyst for MCH dehydrogenation. The results showed no MCH dehydrogenation activity of Sn/Al_2O_3. Therefore, we concluded that itself highly dispersed SnO_x on Al_2O_3 were inert species that were not involved in dehydrogenation of MCH. The TOL selectivity shows an inverse trend to that of the MCH conversion. Upon an increase in the Sn/Pt ratio, there is an increase in the TOL selectivity of the $Pt{-}Sn/Al_2O_3$ catalysts (Figure S10b), where initial TOL selectivities after 5 min of $Pt{-}Sn(3)/Al_2O_3$ and Pt/Al_2O_3 were the highest (100.0%) and the lowest (99.85%) among all of the catalysts, respectively. Next, the durability of the catalysts was evaluated based on the time courses of their MCH conversions. For Pt/Al_2O_3, the MCH conversion was observed to rapidly decrease with time, and the MCH conversion reached almost 0 after 65 min. The decay in the MCH conversion for $Pt{-}Sn/Al_2O_3$ decreases upon the addition of Sn to the catalyst, with the final MCH conversion (at 125 min) exhibiting a volcano trend in line with the Sn/Pt ratio (Figure S10c). After 125 min, the MCH dehydrogenation activity of $Pt{-}Sn(2)/Al_2O_3$ was the highest among all of the catalysts. In addition, the $Pt{-}Sn(2)/Al_2O_3$ catalyst even showed high activity after >18 h, especially for the catalytic testing at high MCH conversion. (Figure S12). The deactivation rate of the catalysts was calculated via a pseudo-first-order approximation of the time course of the MCH conversion (Figure S11). As the Sn/Pt ratio increased from 0 to 3, the deactivation rate decreased from 0.69 to 0.02% min^{-1} (Figure S10d). The similar trends in TOL selectivity and durability versus Sn/Pt ratio suggest that the deactivation of the catalysts was as a result of the formation of coke on the catalysts, accompanied by the demethylation of TOL. The coke formed on the catalysts

during the MCH dehydrogenation was analyzed using thermogravimetric analysis (TGA) (Figure S13). Above 500 ºC, at which point the combustion of hard coke occurs, the weight loss values for Pt/Al_2O_3 and $Pt{-}Sn(3)/Al_2O_3$ were 1.7% and 1.1%, respectively. Despite the fact that TOL yield of $Pt{-}Sn(3)/Al_2O_3$ for 120 min (ca. 900 μmol) was greater than that of Pt/Al_2O_3 (ca. 700 μmol), the deposition of hard coke on Pt/Al_2O_3 clearly occurred to a greater extent than on the $Pt{-}Sn(3)/Al_2O_3$.[28] Therefore, the Pt−Sn catalysts which have highly durability can promote the formation of toluene while inhibiting deposition of coke. Furthermore, the test of MCH dehydrogenation−regeneration cycles was performed using $Pt{-}Sn(2)/Al_2O_3$ catalyst. The catalyst sample was regenerated by a flowing of 10% O_2/Ar at 600 °C for 1 h followed by H_2 reduction at 600 °C for 30 min. The regenerated catalyst showed about 80% of the dehydrogenation activity of the fresh catalyst (Figure S14). This result indicated that the catalyst was possible to be regenerated by the combustion of coke.[22] In contrast, the aggregation of nanoparticles was not observed for the Pt/Al_2O_3 and $Pt{-}Sn(1)/Al_2O_3$ catalysts (Figure S15). In addition, as shown in Figure S16, the crystal structures of Pt/Al_2O_3 and $Pt{-}Sn/Al_2O_3$ showed no changes.

As Pt catalysts are rapidly deactivated in the absence of H_2, kinetic analysis of the MCH dehydrogenation was performed in the presence of H_2 (Figure S17 and Table S3). In the presence of 5% H_2, the deactivation rates of all of the catalysts lower than 0.01 % min^{-1}, and their TOL selectivities were all >99.91%. According to the work carried out by Nagatake et al., TOL strongly adsorbs on Pt/Al_2O_3 and thus inhibits the MCH dehydrogenation on this catalyst.[49] Therefore, the suppression of the deactivation of the catalyst in the presence of an excess of H_2 can be attributed to the enhanced desorption of toluene, which is the precursor of coke. In addition, the slightly positive reaction order with respect to H_2 in the MCH dehydrogenation also indicates that toluene is readily desorbed from the catalyst via an H_2-assisted desorption mechanism (Table S2).[50,51] In

the case of the Pt−Sn/Al_2O_3 catalysts, the reaction order with respect to H_2 decreased in line with an increase in the Sn/Pt ratio. A negative reaction order of H_2 suggests that the active sites of the Pt are blocked by H atoms because of the difficulty in desorbing H_2. The reaction order with respect to MCH was 0.7–1.3, which is consistent with that observed for Pt/Al_2O_3 in a previous report (Table S2).[49] Thus, adsorption or C−H activation of MCH on Pt catalysts is the key step in the MCH dehydrogenation.[52]

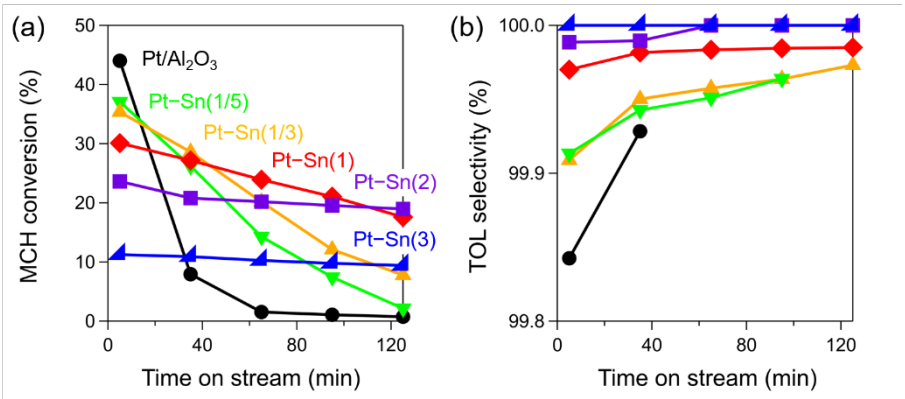

Figure 7. Time on stream of the (a) MCH conversions and (b) TOL selectivities of the Pt/Al_2O_3 and Pt−Sn/Al_2O_3 catalysts. Reaction conditions: catalyst (10 mg), 1.6% MCH/Ar, total flow rate (100 mL min^{-1}), GHSV (600,000 mL g^{-1} h^{-1}), and 300 °C.

3.5. Structure−catalytic property relationships of the Pt−Sn/Al_2O_3 catalysts in the MCH dehydrogenation

The TOF for the MCH dehydrogenation can be defined as the reaction rate per molar amount of the surface Pt determined from the CO pulse measurements. Figure S10e shows the initial TOFs

of the Pt−Sn/Al_2O_3 catalysts at 300 °C after 5 min, where it can be seen that the initial TOFs of the catalysts were almost the same, regardless of the Sn/Pt ratio.[28] Therefore, the initial MCH conversion for the Pt−Sn/Al_2O_3 catalysts increases according to an increase in the dispersion of Pt (Figure 8a). Previously, the dehydrogenation of alkanes over the Pt catalysts was well known as a structure-insensitive reaction,[53–55] while more recent paper reported the pivotal role of coordination site of Pt atom which varied by Pt particle size in dehydrogenation of alkanes.[56–58] In this report, the dehydrogenation of MCH over the Pt−Sn catalysts was almost consistent with the former. The size effect of Pt−Sn alloy particles on TOF for dehydrogenation of MCH was not also appeared (Figures S18 and S19 and Table S4). In contrast, the deactivation rate of the Pt−Sn/Al_2O_3 catalysts decreases with a decrease in the fraction of the bridge adsorbed CO on Pt^0 (Figure 8b). In addition, apart from Pt/Al_2O_3, the deactivation rate of Pt−Sn/Al_2O_3 improved in line with an increase in Pt electron density, as estimated from the peak area of the white line of the Pt L_3-edge (Figure S20). According to the work by Nakaya et al., the adsorption of TOL on the surface of Pt_3Sn is weaker than that on the surface Pt due to the difference in the orientation of the molecule upon adsorption to the respective materials.[28] Electron-rich Pt promotes the desorption of TOL, which is the precursor of coke, due to in enhancement in the electronic repulsion that arises between Pt and TOL.[28,49] Therefore, the addition of Sn into a catalyst dilutes the Pt nanoparticles, thus inducing a decrease in the number of Pt−Pt adjacent sites and an increase in the Pt electron density, which enhance the durability and TOL selectivity in the MCH dehydrogenation. From the data shown in Figures 8b and S18, it can be seen that the deactivation rate is strongly correlated with the fraction of the bridge adsorbed CO on Pt^0 or the peak area of white line, which suggests that the geometric and electronic structure which are changed by the addition of Sn play a more important role in the durability of the catalysts. Thus, the above results concluded that the number

of surface Pt atoms and the local structure of these atoms, which vary according to the size and crystal structure of the Pt−Sn nanoparticles, are the controlling factors that underpin the properties of the catalysts in the MCH dehydrogenation.

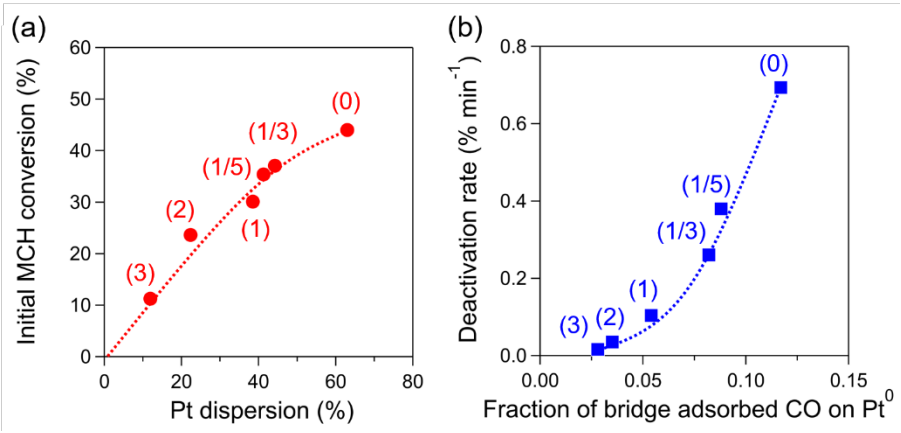

Figure 8. Dependence of (a) the initial conversion of MCH and (b) the deactivation rate on the dispersion of Pt and fraction of bridge CO adsorbed on Pt^0 in the Pt/Al_2O_3 and $Pt–Sn/Al_2O_3$ catalysts. The Sn/Pt ratio of the Pt/Al_2O_3 and $Pt–Sn/Al_2O_3$ catalysts are shown in parentheses.

4. CONCLUSIONS

A systematic investigation was carried out to determine the relationship between the structure and catalytic performance of $Pt–Sn/Al_2O_3$ samples with different Sn/Pt ratios in the dehydrogenation of MCH. Upon an increase in the Sn/Pt ratio, structural changes in the catalysts were observed from the presence of Pt−Sn clusters to intermetallic Pt_3Sn and PtSn nanoparticles. The dispersion of Pt, the number of the Pt ensemble sites, and the electronic state of Pt was also observed to change in line with the Sn/Pt ratio. More specifically, the dispersion of Pt and the fraction of Pt−Pt

adjacent sites monotonically decreased with the increasing Sn content of the catalysts. The electron density of Pt in the catalysts increased due to the charge transfer that occurred from Sn to Pt. Overall, it was found that the catalytic performance of the different Pt−Sn/Al_2O_3 catalysts in the dehydrogenation of MCH was limited by the trade-off between the initial activity and selectivity−durability of the materials. The initial MCH activity was found to be dependent on the dispersion of Pt in the catalysts. However, the TOL selectivity and durability of the catalysts could be correlated to a decrease in the number of adjacent Pt sites and a subsequent increase in the electron density of Pt. Among all the catalysts presented in this study, Pt−Sn(2)/Al_2O_3 showed best catalytic performance in terms of both initial activity and selectivity−durability. It is believed that the nanostructure−catalytic property relationships identified in this study will advance the precise design of Pt-based catalysts not only for use in the dehydrogenation of MCH, but also in the industrial dehydrogenation of alkanes.

ASSOCIATED CONTENT

Supporting Information.

The following files are available free of charge.

Curve fitting results of Pt L_3-edge FTs of EXAFS spectra, curve fittings of Pt L_3-edge XANES spectra, Sn K-edge XANES, EXAFS, and FTs of EXAFS spectra, wavenumber of linear adsorbed CO on Pt−Sn/Al_2O_3 catalysts, Fittings of the IR spectra of adsorbed CO with Gaussian functions, dependence of the initial MCH conversion, initial TOL selectivity, and final MCH conversion for Pt−Sn/Al_2O_3 catalysts on the Sn/Pt ratio, long-term of MCH dehydrogenation test, TGA analysis

of the catalysts after MCH dehydrogenation, TEM images of the catalysts after MCH dehydrogenation, XRD patterns of the catalysts after MCH dehydrogenation, dependence of TOF on partial pressure of MCH and H_2 for MCH dehydrogenation, reaction order with respect to MCH and H_2 partial pressure for the MCH dehydrogenation, dependence of deactivation rate on peak area of white line for Pt L_3-edge XANES spectra of the catalysts (PDF)

AUTHOR INFORMATION

Corresponding Author

*E-mail: satsuma@chembio.nagoya-u.ac.jp.

Notes

The authors declare no competing financial interest.

ACKNOWLEDGMENT

This work was partly supported by the JSPS KAKENHI Grant- in-Aids for Scientific Research (B) (Grant Nos. 18H01787) and JSPS Fellows (Grant Nos. 19J15440) from the Ministry of Education, Culture, Sports, Science and Technology (MEXT), Japan. A part of this work was managed by the Elements Strategy Initiative for Catalysts & Batteries (ESICB, JPMXP0112101003), which is also supported by MEXT. XAFS measurement was conducted at BL5S1 and BL11S2 of Aichi Synchrotron Radiation Center, Aichi & Technology Foundation (Approval No. 202003020, 202003056, and 202004017). The authors would like to thank Enago (www.enago.jp) for English language review.

ABBREVIATIONS

MCH, methylcyclohexane; STEM, scanning transmission electron microscopy; XAFS, X-ray absorption fine structure; IR, infrared; TOL, toluene; TOF, turnover frequency; FT, Fourier-transform; CO, Carbon monoxide; EDS, energy-dispersive X-ray spectroscopy; Cs, spherical aberration-corrected; EELS, electron energy loss spectroscopy; GHSV, gas hourly space velocity; BID, dielectric-barrier discharge ionization detector; CH_4, methane; XANES, X-ray absorption near edge structure; TGA, thermogravimetric analysis

REFERENCES

(1) Sattler, J. J. H. B.; Ruiz-Martinez, J.; Santillan-Jimenez, E.; Weckhuysen, B. M. Catalytic Dehydrogenation of Light Alkanes on Metals and Metal Oxides. *Chem. Rev.* **2014**, *114*, 10613–10653.

(2) Saito, H.; Sekine, Y. Catalytic Conversion of Ethane to Valuable Products through Non-Oxidative Dehydrogenation and Dehydroaromatization. *RSC Adv.* **2020**, *10*, 21427–21453.

(3) Okada, Y.; Sasaki, E.; Watanabe, E.; Hyodo, S.; Nishijima, H. Development of Dehydrogenation Catalyst for Hydrogen Generation in Organic Chemical Hydride Method. *Int. J. Hydrogen Energy* **2006**, *31*, 1348–1356.

(4) Gianotti, E.; Taillades-Jacquin, M.; Rozière, J.; Jones, D. J. High-Purity Hydrogen Generation via Dehydrogenation of Organic Carriers: A Review on the Catalytic Process. *ACS Catal.* **2018**, *8*, 4660–4680.

(5) Deng, L.; Shishido, T.; Teramura, K.; Tanaka, T. Effect of Reduction Method on the Activity of Pt-Sn/SiO_2 for Dehydrogenation of Propane. *Catal. Today* **2014**, *232*, 33–39.

(6) Deng, L.; Miura, H.; Shishido, T.; Hosokawa, S.; Teramura, K.; Tanaka, T. Dehydrogenation of Propane over Silica-Supported Platinum-Tin Catalysts Prepared by Direct Reduction: Effects of Tin/Platinum Ratio and Reduction Temperature. *ChemCatChem* **2014**, *6*, 2680–2691.

(7) Deng, L.; Miura, H.; Shishido, T.; Wang, Z.; Hosokawa, S.; Teramura, K.; Tanaka, T. Elucidating Strong Metal-Support Interactions in Pt–Sn/SiO_2 Catalyst and Its Consequences for Dehydrogenation of Lower Alkanes. *J. Catal.* **2018**, *365*, 277–291.

(8) Jung, J. W.; Kim, W. Il; Kim, J. R.; Oh, K.; Koh, H. L. Effect of Direct Reduction Treatment on Pt–Sn/Al2O3 Catalyst for Propane Dehydrogenation. *Catalysts* **2019**, *9*, 446.

(9) Shi, L.; Deng, G. M.; Li, W. C.; Miao, S.; Wang, Q. N.; Zhang, W. P.; Lu, A. H. Al_2O_3 Nanosheets Rich in Pentacoordinate Al^{3+} Ions Stabilize Pt-Sn Clusters for Propane Dehydrogenation. *Angew. Chem. Int. Ed.* **2015**, *54*, 13994–13998.

(10) Jang, E. J.; Lee, J.; Jeong, H. Y.; Kwak, J. H. Controlling the Acid-Base Properties of Alumina for Stable PtSn-Based Propane Dehydrogenation Catalysts. *Appl. Catal. A Gen.* **2019**, *572*, 1–8.

(11) Zhang, J.; Deng, Y.; Cai, X.; Chen, Y.; Peng, M.; Jia, Z.; Jiang, Z.; Ren, P.; Yao, S.; Xie, J.; Xiao, D.; Wen, X.; Wang, N.; Liu, H.; Ma, D. Tin-Assisted Fully Exposed Platinum Clusters Stabilized on Defect-Rich Graphene for Dehydrogenation Reaction. *ACS Catal.* **2019**, *9*, 5998–6005.

(12) Liu, L.; Lopez-Haro, M.; Lopes, C. W.; Li, C.; Concepcion, P.; Simonelli, L.; Calvino, J. J.; Corma, A. Regioselective Generation and Reactivity Control of Subnanometric Platinum Clusters in Zeolites for High-Temperature Catalysis. *Nat. Mater.* **2019**, *18*, 866–873.

(13) Xu, Z.; Yue, Y.; Bao, X.; Xie, Z.; Zhu, H. Propane Dehydrogenation over Pt Clusters Localized at the Sn Single-Site in Zeolite Framework. *ACS Catal.* **2020**, *10*, 818–828.

(14) Liu, L.; Lopez-Haro, M.; Lopes, C. W.; Rojas-Buzo, S.; Concepcion, P.; Manzorro, R.; Simonelli, L.; Sattler, A.; Serna, P.; Calvino, J. J.; Corma, A. Structural Modulation and Direct Measurement of Subnanometric Bimetallic PtSn Clusters Confined in Zeolites. *Nat. Catal.* **2020**, *3*, 628–638.

(15) Balakrishnan, K.; Schwank, J. FTIR Study of Bimetallic Pt-Sn/Al_2O_3 Catalysts. *J. Catal.* **1992**, *138*, 491–499.

(16) Lee, M. H.; Nagaraja, B. M.; Lee, K. Y.; Jung, K. D. Dehydrogenation of Alkane to Light Olefin over PtSn/θ-Al_2O_3 Catalyst: Effects of Sn Loading. *Catal. Today* **2014**, *232*, 53–62.

(17) De Ménorval, L. C.; Chaqroune, A.; Coq, B.; Figueras, F. Characterization of Mono- and Bi-Metallic Platinum Catalysts Using CO FTIR Spectroscopy: Size Effects and Topological Segregation. *J. Chem. Soc. - Faraday Trans.* **1997**, *93*, 3715–3720.

(18) Uemura, Y.; Inada, Y.; Bando, K. K.; Sasaki, T.; Kamiuchi, N.; Eguchi, K.; Yagishita, A.; Nomura, M.; Tada, M.; Iwasawa, Y. Core-Shell Phase Separation and Structural Transformation of Pt_3Sn Alloy Nanoparticles Supported on γ-Al_2O_3 in the Reduction and Oxidation Processes Characterized by in Situ Time-Resolved XAFS. *J. Phys. Chem. C* **2011**, *115*, 5823–5833.

(19) Caballero, A.; Dexpert, H.; Didillon, B.; LePeltier, F.; Clause, O.; Lynch, J. In Situ X-Ray Absorption Spectroscopic Study of a Highly Dispersed PtSn/Al_2O_3 Catalyst. *J. Phys. Chem.* **1993**, *97*, 11283–11285.

(20) Borgna, A.; Stagg, S. M.; Resasco, D. E. Interference Phenomena in the EXAFS Spectra of Pt-Sn Bimetallic Catalysts. *J. Phys. Chem. B* **1998**, *102*, 5077–5081.

(21) Moscu, A.; Theodoridi, C.; Cardenas, L.; Thieuleux, C.; Motta-Meira, D.; Agostini, G.; Schuurman, Y.; Meunier, F. CO Dissociation on Pt-Sn Nanoparticles Triggers Sn Oxidation and Alloy Segregation. *J. Catal.* **2018**, *359*, 76–81.

(22) Pham, H. N.; Sattler, J. J. H. B.; Weckhuysen, B. M.; Datye, A. K. Role of Sn in the Regeneration of Pt/γ-Al_2O_3 Light Alkane Dehydrogenation Catalysts. *ACS Catal.* **2016**, *6*, 2257–2264.

(23) Iglesias-juez, A.; Beale, A. M.; Maaijen, K.; Chien, T.; Glatzel, P.; Weckhuysen, B. M. A Combined in Situ Time-Resolved UV–Vis , Raman and High-Energy Resolution X-Ray Absorption Spectroscopy Study on the Deactivation Behavior of Pt and Pt A Sn Propane

Dehydrogenation Catalysts under Industrial Reaction Conditions. *J. Catal.* **2010**, *276*, 268–279.

(24) Kaylor, N.; Davis, R. J. Propane Dehydrogenation over Supported Pt-Sn Nanoparticles. *J. Catal.* **2018**, *367*, 181–193.

(25) Deng, L.; Arakawa, T.; Ohkubo, T.; Miura, H.; Shishido, T.; Hosokawa, S.; Teramura, K.; Tanaka, T. Highly Active and Stable Pt-Sn/SBA-15 Catalyst Prepared by Direct Reduction for Ethylbenzene Dehydrogenation: Effects of Sn Addition. *Ind. Eng. Chem. Res.* **2017**, *56*, 7160–7172.

(26) Furukawa, S.; Tamura, A.; Ozawa, K.; Komatsu, T. Catalytic Properties of Pt-Based Intermetallic Compounds in Dehydrogenation of Cyclohexane and n-Butane. *Appl. Catal. A Gen.* **2014**, *469*, 300–305.

(27) Wu, J.; Peng, Z.; Bell, A. T. Effects of Composition and Metal Particle Size on Ethane Dehydrogenation over Pt_xSn_{100-x}/Mg(Al)O ($70 \leq x \leq 100$). *J. Catal.* **2014**, *311*, 161–168.

(28) Nakaya, Y.; Miyazaki, M.; Yamazoe, S.; Shimizu, K.; Furukawa, S. Active, Selective, and Durable Catalyst for Alkane Dehydrogenation Based on a Well-Designed Trimetallic Alloy. *ACS Catal.* **2020**, *10*, 5163–5172.

(29) Nakaya, Y.; Hirayama, J.; Yamazoe, S.; Shimizu, K. ichi; Furukawa, S. Single-Atom Pt in Intermetallics as an Ultrastable and Selective Catalyst for Propane Dehydrogenation. *Nat. Commun.* **2020**, *11*, 3–9.

(30) Zangeneh, F. T.; Mehrazma, S.; Sahebdelfar, S. The Influence of Solvent on the Performance of Pt-Sn/θ-Al2O3 Propane Dehydrogenation Catalyst Prepared by Co-Impregnation Method. *Fuel Process. Technol.* **2013**, *109*, 118–123.

(31) Alcock, N. W.; Nelson, J. H. The $[PtCl_2(SnCl_3)_2]^{2-}$ Ion: Crystal Structure of Two Salts. *J. Chem. Soc. Dalt. Trans.* **1982**, *2*, 2415–2418.

(32) Shekhar, M.; Wang, J.; Lee, W.; Williams, W. D.; Kim, S. M.; Stach, E. A.; Miller, J. T.; Delgass, W. N.; Ribeiro, F. H. Size and Support Effects for the Water−Gas Shift Catalysis over Gold. *J. Am. Chem. Soc.* **2012**, *134*, 4700–4708.

(33) Borges, L. R.; Lopez-Castillo, A.; Meira, D. M.; Gallo, J. M. R.; Zanchet, D.; Bueno, J. M. C. Effect of the Pt Precursor and Loading on the Structural Parameters and Catalytic Properties of Pt/Al_2O_3. *ChemCatChem* **2019**, *11*, 3064–3074.

(34) Chizallet, C.; Sautet, P.; Raybaud, P. Platinum Nanoclusters Stabilized on γ -Alumina by Chlorine Used As a Capping Surface Ligand: A Density Functional Theory Study. *ACS Catal.* **2012**, *2*, 1346−1357.

(35) Yoshida, H.; Nonoyama, S.; Yazawa, Y.; Hattori, T. Quantitative Determination of Platinum Oxidation State by XANES Analysis. *Phys. Scr. T* **2005**, *T115*, 813–815.

(36) Mansour, A. N.; Cook, J. W.; Sayers, D. E. Quantitative Technique for the Determination of the Number of Unoccupied D-Electron States in a Platinum Catalyst Using the $L_{2,3}$ X-Ray Absorption Edge Spectra. *J. Phys. Chem.* **1984**, *88*, 2330–2334.

(37) Shimizu, K. I.; Kamiya, Y.; Osaki, K.; Yoshida, H.; Satsuma, A. The Average Pd Oxidation State in Pd/SiO_2 Quantified by L_3-Edge XANES Analysis and Its Effects on Catalytic Activity for CO Oxidation. *Catal. Sci. Technol.* **2012**, *2*, 767–772.

(38) Vila, F. D.; Rehr, J. J.; Kelly, S. D.; Bare, S. R. Operando Effects on the Structure and Dynamics of $Pt_nSn_m/\gamma\text{-}Al_2O_3$ from Ab Initio Molecular Dynamics and X-Ray Absorption Spectra. *J. Phys. Chem. C* **2013**, *117*, 12446–12457.

(39) Vaarkamp, M.; Miller, J. T.; Modica, F. S.; Koningsberger, D. C. On the Relation between Particle Morphology , Structure of the Metal-Support Interface , and Catalytic Properties of $Pt/\gamma\text{-}Al_2O_3$. *J. Catal.* **1996**, *163*, 294–305.

(40) Sanchez, S. I.; Menard, L. D.; Bram, A.; Kang, J. H.; Small, M. W.; Nuzzo, R. G.; Frenkel, A. I. The Emergence of Nonbulk Properties in Supported Metal Clusters: Negative Thermal Expansion and Atomic Disorder in Pt Nanoclusters Supported on γ-Al_2O_3. *J. Am. Chem. Soc.* **2009**, No. 11, 7040–7054.

(41) Sinkler, W.; Sanchez, S. I.; Bradley, S. A.; Wen, J.; Mishra, B.; Kelly, S. D.; Bare, S. R. Aberration-Corrected Transmission Electron Microscopy and in Situ XAFS Structural Characterization of Pt/γ-Al_2O_3 Nanoparticles. *ChemCatChem* **2015**, *7*, 3779–3787.

(42) Derita, L.; Dai, S.; Lopez-zepeda, K.; Pham, N.; Graham, G. W.; Pan, X.; Christopher, P. Catalyst Architecture for Stable Single Atom Dispersion Enables Site-Specific Spectroscopic and Reactivity Measurements of CO Adsorbed to Pt Atoms, Oxidized Pt Clusters, and Metallic Pt Clusters on TiO_2. *J. Am. Chem. Soc.* **2017**, *139*, 14150–14165.

(43) Ding, K.; Gulec, A.; Johnson, A. M.; Schweitzer, N. M.; Stucky, G. D.; Marks, L. D.; Stair, P. C. Identification of Active Sites in CO Oxidation and Water-Gas Shift over Supported Pt Catalysts. *Science* **2015**, *350*, 189–192.

(44) Siemer, M.; Tomaschun, G.; Klüner, T.; Christopher, P.; Christopher, P.; Al-Shamery, K. Insights into Spectator-Directed Catalysis: CO Adsorption on Amine-Capped Platinum Nanoparticles on Oxide Supports. *ACS Appl. Mater. Interfaces* **2020**, *12*, 27765–27776.

(45) Kale, M. J.; Christopher, P. Utilizing Quantitative in Situ FTIR Spectroscopy to Identify Well-Coordinated Pt Atoms as the Active Site for CO Oxidation on Al_2O_3-Supported Pt Catalysts. *ACS Catal.* **2016**, *6*, 5599–5609.

(46) Wang, L.; Lu, X.; Wang, W.; Zhan, W.; Guo, Y.; Guo, Y. Identification of Active Sites on High-Performance Pt/Al2O3 Catalyst for Cryogenic CO Oxidation. *ACS Catal.* **2020**, *10*, 8815–8824.

(47) Sattler, A.; Paccagnini, M.; Lanci, M. P.; Miseo, S.; Kliewer, C. E. Platinum Catalyzed C−H Activation and the Effect of Metal−Support Interactions. *ACS Catal.* **2020**, *10*, 710–720.

(48) Singh, J.; Van Bokhoven, J. A. Structure of Alumina Supported Platinum Catalysts of Different Particle Size during CO Oxidation Using in Situ IR and HERFD XAS. *Catal. Today* **2010**, *155*, 199–205.

(49) Nagatake, S.; Higo, T.; Ogo, S.; Sugiura, Y.; Watanabe, R.; Fukuhara, C.; Sekine, Y. Dehydrogenation of Methylcyclohexane over Pt/TiO_2 Catalyst. *Catal. Lett.* **2016**, *146*, 54–60.

(50) Saerens, S.; Sabbe, M. K.; Galvita, V. V.; Redekop, E. A.; Reyniers, M. F.; Marin, G. B. The Positive Role of Hydrogen on the Dehydrogenation of Propane on Pt(111). *ACS Catal.* **2017**, *7*, 7495–7508.

(51) Al-Shaikhali, A. H.; Jedidi, A.; Anjum, D. H.; Cavallo, L.; Takanabe, K. Kinetics on NiZn Bimetallic Catalysts for Hydrogen Evolution via Selective Dehydrogenation of Methylcyclohexane to Toluene. *ACS Catal.* **2017**, *7*, 1592–1600.

(52) Zhao, W.; Chizallet, C.; Sautet, P.; Raybaud, P. Dehydrogenation Mechanisms of Methyl-Cyclohexane on γ-Al_2O_3 Supported Pt_{13}: Impact of Cluster Ductility. *J. Catal.* **2019**, *370*, 118–129.

(53) Breysse, M.; Frety, R. Resistance to Sulfur Poisoning of Metal Catalysts. *J. Catal.* **1987**, *154*, 144–154.

(54) Cusumano, J. A.; Dembinski, G. W.; Sinfelt, J. H. Chemisorption and Catalytic Properties of Supported Platinum. *J. Catal.* **1966**, *5*, 471–475.

(55) Boudart, M. Catalysis by Supported Metals. *Adv. Catal.* **1969**, *20*, 153–166.

(56) Somorjai, G. A.; Park, J. Y. Molecular Surface Chemistry by Metal Single Crystals and Nanoparticles from Vacuum to High Pressure. *Chem. Soc. Rev.* **2008**, *37*, 2155–2162.

(57) Rioux, R. M.; Hsu, B. B.; Grass, M. E.; Song, H.; Somorjai, G. A. Influence of Particle Size on Reaction Selectivity in Cyclohexene Hydrogenation and Dehydrogenation over Silica-Supported Monodisperse Pt Particles. *Catal. Lett.* **2008**, *126*, 10–19.

(58) Zhu, J.; Yang, M. L.; Yu, Y.; Zhu, Y. A.; Sui, Z. J.; Zhou, X. G.; Holmen, A.; Chen, D. Size-Dependent Reaction Mechanism and Kinetics for Propane Dehydrogenation over Pt Catalysts. *ACS Catal.* **2015**, *5*, 6310–6319.

TOC

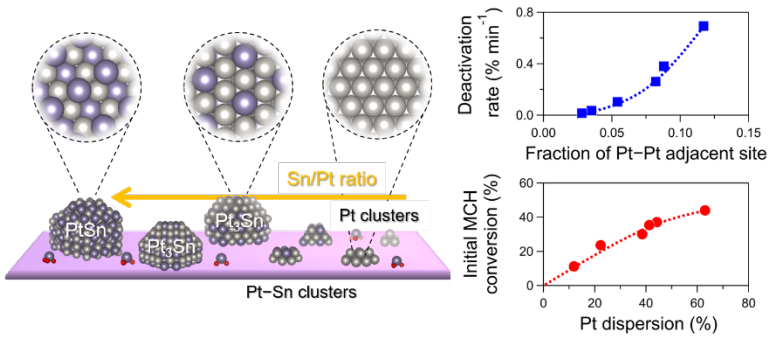
Sn/Pt ratio
Pt clusters
PtSn
Pt3Sn
Pt3Sn
Pt−Sn clusters
Deactivation rate (% min-1)
0.8
0.4
0.0
0.00
0.05
0.10
0.15
Fraction of Pt−Pt adjacent site
Initial MCH conversion (%)
60
40
20
0
0
20
40
60
80
Pt dispersion (%)